frontiers | Frontiers in Earth Science

TYPE Original Research
PUBLISHED 20 September 2024
DOI 10.3389/feart.2024.1423174

OPEN ACCESS

EDITED BY
Paolo Capuano,
University of Salerno, Italy

REVIEWED BY
Andrea Billi,
National Research Council (CNR), Italy
Carlos Peña,
GFZ German Research Centre for Geosciences, Germany

*CORRESPONDENCE
Valentin Marguin,
✉ valentin.marguin@icloud.com

RECEIVED 25 April 2024
ACCEPTED 21 August 2024
PUBLISHED 20 September 2024

CITATION
Marguin V and Simpson G (2024) Poroelastic effects associated with earthquakes on overpressured reverse and normal faults.
Front. Earth Sci. 12:1423174.
doi: 10.3389/feart.2024.1423174

Poroelastic effects associated with earthquakes on overpressured reverse and normal faults

Valentin Marguin* and Guy Simpson

Department of Earth Sciences, University of Geneva, Geneva, Switzerland

Earthquakes in fluid-saturated rocks induce sudden changes in pore-pressures that can lead to appreciable postseismic deformation. However, earthquakes can also release fluids from overpressured parts of the crust, which can also contribute to additional postseismic effects. In this study, we use two-dimensional poroelastic models to investigate postseismic deformation and fluid pressures following ruptures on overpressured dip-slip faults that slide according to rate- and state-dependent friction. We show that when the crust prior to rupture has pore pressures in hydrostatic equilibrium, then ruptures induce fluid pressure anomalies according to the field of coseismic elastic volumetric strain. These pore pressure anomalies relax with time to produce characteristic postseismic deformation that depends on the slip magnitude and fault style, as typically observed. However, very different results are obtained if the crust is appreciably overpressured at the time an earthquake is nucleated. In this case, the poroelastic response is overwhelmingly dominated by drainage and fluid pressure drop within the overpressured crust, which is facilitated by an increase in permeability on the fault during rupture. This results in transient postseismic subsidence that occurs irrespective of the faulting style, fault geometry, slip magnitude or details of the coseismic strain field. The time scale and magnitude of this postseismic subsidence are controlled by the magnitude of the fluid overpressure prior to rupture, the maximum coseismic permeability and how rapidly the fault permeability recovers following an earthquake. The poroelastic effects associated with rupturing of overpressured faults may be at least an order of magnitude greater that the classic poroelastic response (i.e., relaxation of pore pressures generated by coseismic elastic volumetric strain). Overall, our results highlight the potentially dramatic effect that the breaching of deep overpressured fluid reservoirs can have on fluid pressures and surface displacements following earthquakes.

KEYWORDS

poroelasticity, earthquakes, fluid pressure, permeability and porosity, numerical modelling

1 Introduction

After a major earthquake, surface deformation is influenced by many postseismic processes occurring at different spatial and temporal scales. These processes include postseismic slip along the fault plane (Shrivastava et al., 2016; Freed et al., 2017; Huang et al., 2017; Guo et al., 2019a), viscoelastic relaxation in the lower crust and

TABLE 1 Model parameters.

Parameter	Symbol	Value
Domain dimension	D_z, D_x	30 km, 80 km
Fault dip		30°
Boundary velocity	V_B	25 mm/yr
Shear modulus	μ	30 GPa
Gravity	g	9.81 m/s^2
Rock density	ρ	2,700 kg/m^3
Fluid density	ρ_f	1,000 kg/m^3
Biot's coefficient	α	1
Fluid viscosity	η_f	1.83.10^{-4} Pa.s
Effective bulk compressibility	β	5.10^{-11} Pa^{-1}
Fluid Source parameter	γ	20 km
Fluid source parameter	S_0	0 - 10^{-13} (kg_{H_2O}) $(kg_{rock})^{-1}$ s^{-1}
Permeability parameter	σ^*	30 MPa
Healing time scale	T_H	2 years
Sliding time scale	T_S	1 s
Maximum fault permeability	k_{max}	$10^{-8} - 10^{-12}$ m^2
Critical sliding velocity	V_c	10^{-3} m/s
Direct effect parameter	a	0.015
State evolution parameter	b	see Figure 2B
State evolution distance	d_c	0.025 m
Reference velocity	V_0	10^{-6} m/s
Reference friction coefficient	f_0	0.6
Shear wave speed	C_s	$\sqrt{\mu/\rho}$
Radiation damping term	Ω	$\mu/2C_s$

underlying mantle (Freed and Lin, 2001; Guo et al., 2019b; Peña et al., 2020), and poroelastic deformation due to the migration of pressurized pore fluids (Peltzer et al., 1996; 1998; Jónsson et al., 2003). Most previous research on poroelastic effects (e.g. (Peltzer et al., 1996; 1998; Jónsson et al., 2003)) has focused on how pore pressure changes that result from coseismic faulting induce time-dependent postseismic deformation. In this research, we focus on the poroelastic response linked to earthquakes on overpressurised dip-slip faults, especially immediately following large ruptures.

When an earthquake occurs in a fluid-saturated porous medium, changes in mean stress resulting from differential displacements may induce variations in pore fluid pressure in the surrounding crust. These fluid pressure anomalies then relax, inducing time-dependent displacement, a phenomenon known as poroelastic rebound (Segall, 2010). Depending on the permeability of the rocks, poroelastic rebound can last for months (Jónsson et al., 2003; Árnadóttir et al., 2005), or even years (Fialko, 2004). Understanding the poroelastic response induced by earthquakes is essential because it may control stress transfer, earthquake triggering and afterschocks (Freed and Lin, 2001; Miller et al., 2004; Hughes et al., 2010).

Poroelastic rebound is generally thought to be strongly linked to the tectonic regime and style of faulting (Muir-Wood and King, 1993; Segall, 2010; Doglioni et al., 2014). For example, in the case of normal faulting, dilational volumetric coseismic strain in the handingwall block close to the surface is expected to reduce fluid pressures whereas contractional strain in the footwall block will tend to increase pore pressures (Segall, 2010). Relaxation of these pore fluid pressures anomalies following rupture may then result in additional deformation. The opposite is expected for reverse faulting. No changes in mean stress will occur adjacent to infinitely long strike-slip faults. However, finite length strike slip faults will perturb volumetric strain in the vicinity of fault tips (or fault jogs), which may induce significant poroelastic effects [e.g., see Jónsson et al. (2003)].

Although some observations of pore pressure changes and postseismic deformation are broadly consistent with coseismic strain fields (Muir-Wood and King, 1993; Quilty and Roeloffs, 1997; Jónsson et al., 2003; Akita and Matsumoto, 2004), other studies indicate a more complicated picture (Wang and Manga, 2015). For example, following the 1999 M7.5 Chi-Chi earthquake in Taiwan, most wells experienced a coseismic increase in water levels where the strain field should have caused dilation (Koizumi et al., 2004; Wang et al., 2001). Cox et al. (2021) suggested that earthquake-induced liquefaction and changes in well levels following the 2010 Darfield earthquake in New Zealand indicate that porous flow is not generated by the coseismic displacement field but by the breaching of an overpressured fluid reservoir at depth, facilitated by an abrupt change in coseismic permeability. Similar conclusions have been made by Miller et al. (2004) and Terakawa et al. (2010). These interpretations are consistent with the general view that some faults may act as pressure valves, opening abruptly during earthquakes, thus enabling fluid overpressures to dissipate, before closing by mineral precipitation during the interseismic period (Sibson, 1990).

In this study, we investigate how drainage from overpressured fault zones during and immediately following rupture impacts on the displacement and pressure fields in the surrounding crust. Our analysis is based on a two dimensional numerical model of poroelastic deformation associated with reverse and normal faults that rupture according to rate- and state-dependent friction. Our model includes classic poroelastic effects generated in response to coseismic volumetric strain, as modeled previously by others (Peltzer et al., 1996; 1998; Jónsson et al., 2003). In addition, we consider that faults are overpressured at the time of rupture and that permeability on the fault increases sharply during an earthquake before decreasing postseismically. Our objectives are to understand how these phenomena influence the poroelastic response in comparison to the classic theory. We do not consider why or how fluid overpressures in the crust may be generated,

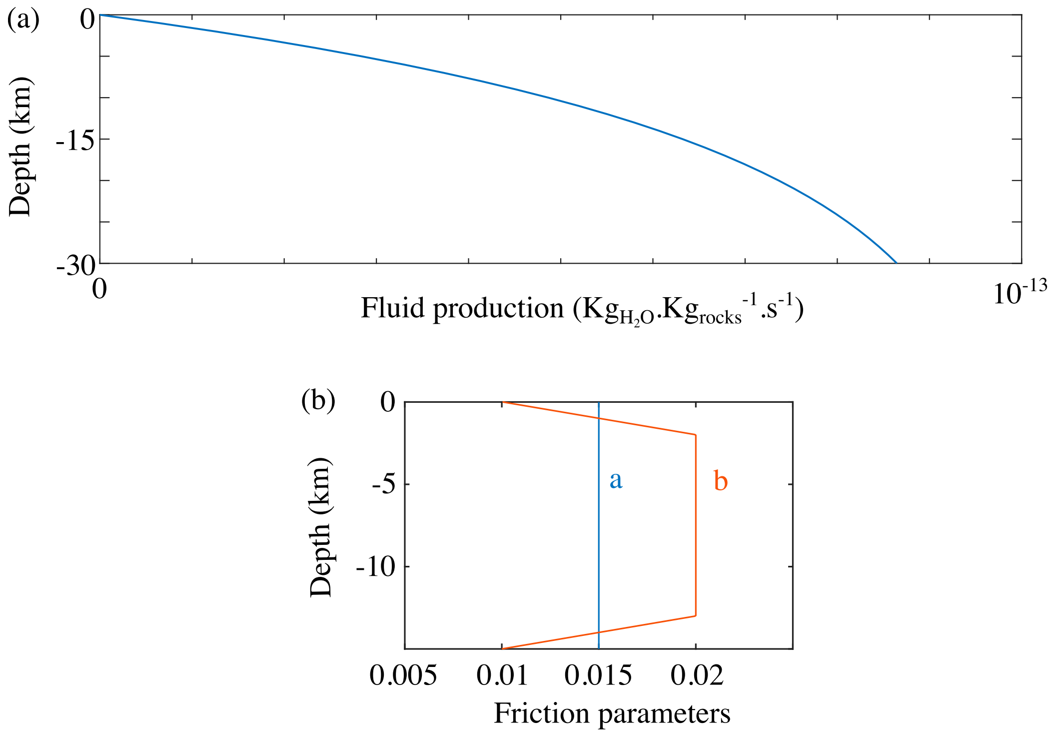

FIGURE 1
(A) Fluid production rate in model with $S_0 = 10^{-13}$ (kg H_2O) (kg Rock)$^{-1}$ s^{-1} (see Equation 9). **(B)** Rate and state friction parameters on the fault (see Equation 6).

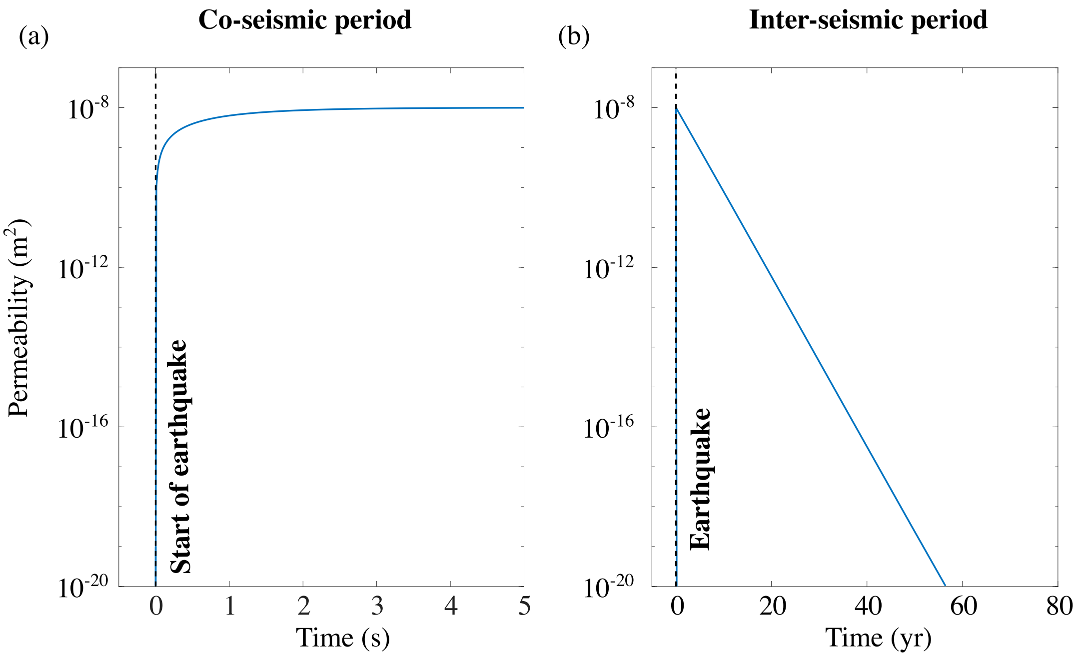

FIGURE 2
Illustration of permeability evolution (see Equation 11) on the fault during **(A)** coseismic period (when $V_f > V_c$) and **(B)** postseismic-interseismic period (when $V_f < V_c$). In this example, $k_{max} = 10^{-8}$ m^{-2}, $T_S = 1$ s and $T_H = 2$ years. The actual permeability variation during a model rupture can be significantly more complicated.

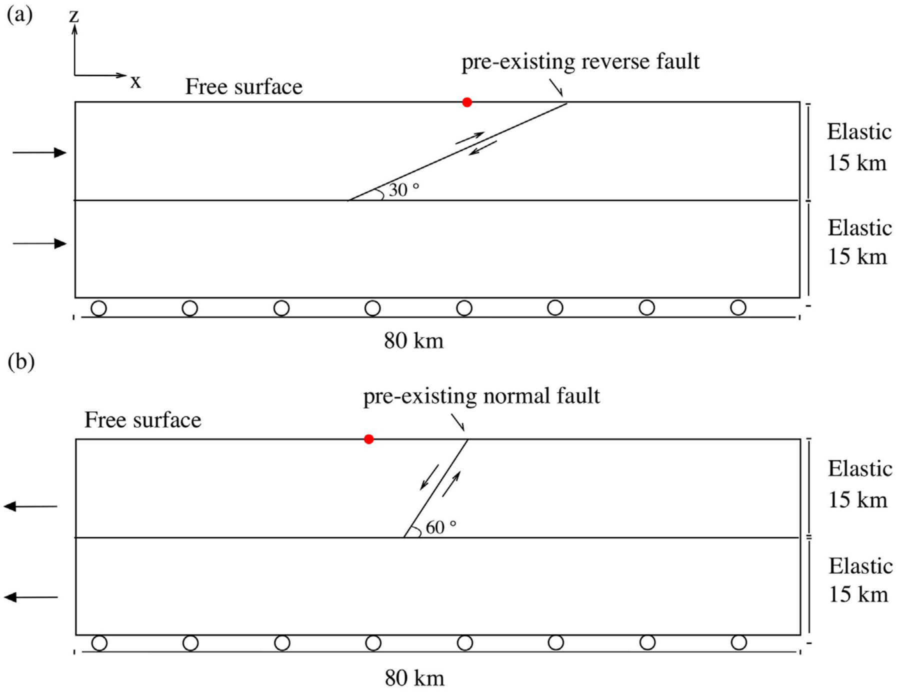

FIGURE 3
Geometry of the model, consisting of an elastic layer with an embedded discrete planar fault. For convergent experiments **(A)** we assume that the fault has a dip of 30°, while for extensional experiments **(B)** the fault has a dip of 60°, implying that faults are optimally oriented for frictional sliding (assuming a background friction angle of 30°). Figures 10–13 show surface displacements at locations indicated by red dots.

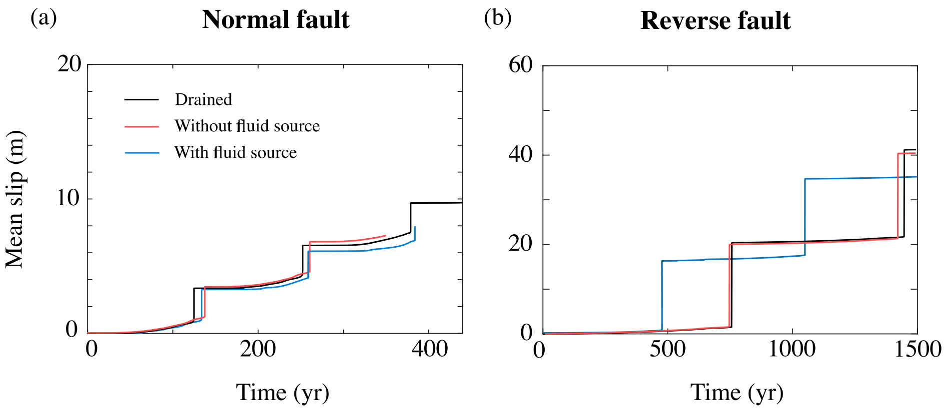

FIGURE 4
Mean slip for a normal fault **(A)** and reverse fault **(B)** encompassing 3 simulations: fully drained (black curve), no pre-rupture fluid overpressure (red curve) and with a pre-rupture fluid overpressure (blue curve).

which may involve a variety of processes including devolatisation reactions (Connolly, 1997), magmatic dewatering (Norton, 1984) or compaction (Walder and Nur, 1984). Additionally, we have not incorporated additional features that may lead to postseismic deformation such as viscoelastic deformation or postseismic fault afterslip. These features are omitted only in order to highlight the poroelastic response, not because we believe them to be unimportant.

2 Methodology

Our model considers two dimensional poroelastic deformation adjacent to a predefined normal or reverse fault that slips according to rate-state friction. Faults with background friction coefficients of 0.6 are assumed to be optimally oriented with respect to frictional sliding. Thus, for convergent experiments, the reverse fault has a dip of about 30°, while in extension, the normal fault has a dip of close to

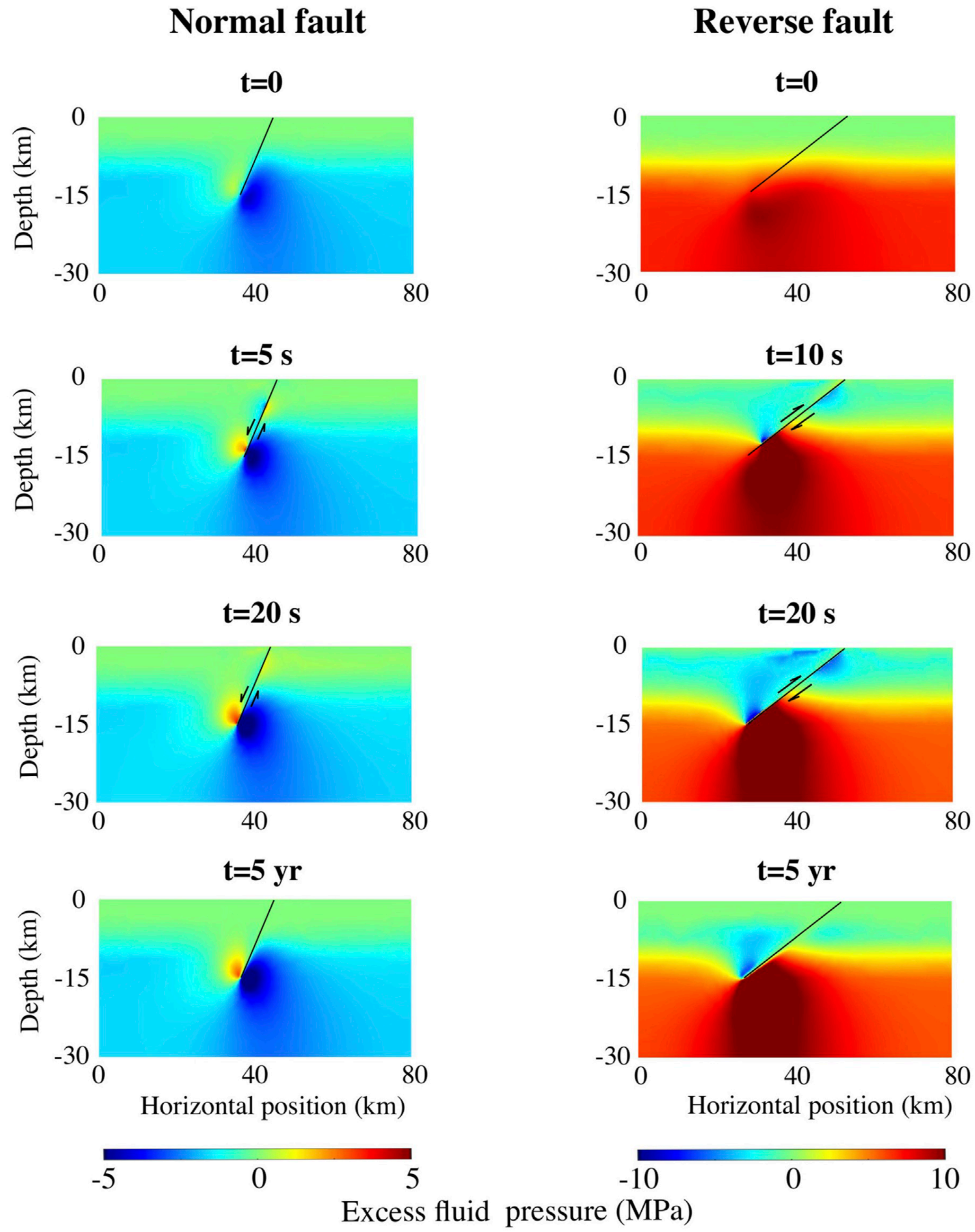

FIGURE 5
Snapshots of the fluid overpressure at different times shortly before, during, and after ruptures on normal (left) and reverse (right) faults in simulations with no pre-rupture fluid overpressure (i.e., without fluid source, $S_0 = 0$). The model domain in each panel is 80 km wide and 30 km deep. All times indicated are relative to the onset of rupture. The black line in each panel indicates the fault plane.

60°. Faulting is assumed to be confined to the upper half of an elastic layer that has a total thickness of 30 km.

Our model is a variant of that already presented by Marguin and Simpson (2023). It is based on quasi-static force balance, which in two-dimensions can be written as

$$\nabla^T \left(\sigma' - \alpha m P_f\right) = -[0, 0, -\rho g]^T \tag{1}$$

where ∇ is the gradient operator, σ' is the effective stress vector (using Voigt notation), α is Biot's coefficient, m is the vector form of kronecker's delta (δ_{ij}), P_f is fluid pressure, ρ is rock density, and g is the acceleration due to gravity (see Table 1 for notation).

The stress-strain relation for an isotropic elastic material can be written as

$$\frac{\partial \sigma'}{\partial t} = D \frac{\partial \epsilon}{\partial t} \tag{2}$$

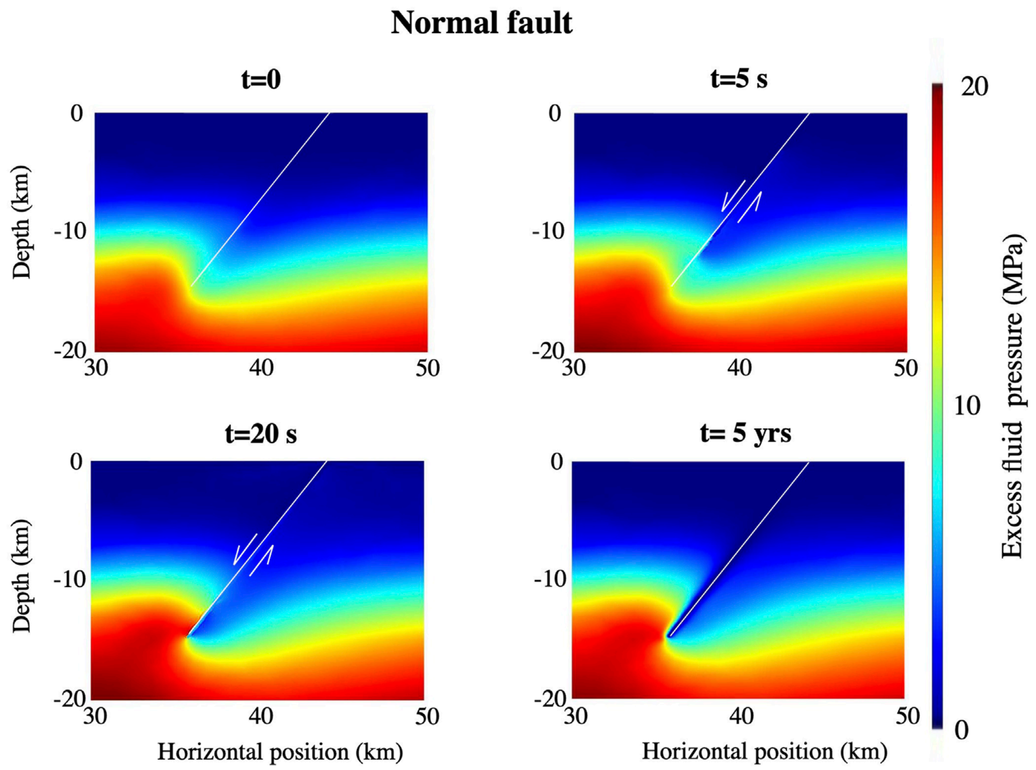

FIGURE 6
Snapshots of the fluid overpressure at different times shortly before, during, and after a large mainshock on a normal fault with a preexisting fluid overpressure due to fluid production (S_0 = 7.5 x 10^{-14} s^{-1}). Only the part of the model close to the fault (20 km wide and 20 km deep) is shown. The white line in each panel indicates the fault plane.

where D and ϵ is the strain vector. The kinematic relation between strains and velocities (assuming small strains) can be written as

$$\frac{\partial \epsilon}{dt} = \nabla V \tag{3}$$

where V the velocity vector. Combining the last two equations (i.e., Equations 2, 3), gives

$$\frac{\partial \sigma'}{\partial t} = D \nabla V \tag{4}$$

We discretise this equation using a forward Euler finite difference approximation and substitute it into Equation 1 to leave a system of equations with velocities and fluid pressure as the unknowns.

Fault motion is governed by Coulomb behaviour combined with rate- and state-dependent friction. Here, the Coulomb condition is modified to account for radiation damping:

$$\tau = f\left(V_f, \theta\right) \boldsymbol{\sigma}'_n + \Omega V_f \tag{5}$$

where τ is the shear stress, σ'_n is the effective normal stress, Ω is the radiation damping term (where $\Omega = \mu/2c_s$, with μ is the shear modulus and c_s is the shear wave speed) and $f(V_f, \theta)$ is the friction coefficient that is given by (Dieterich, 1979; Ruina, 1983; Marone, 1998)

$$f\left(V_f, \theta\right) = f_o + a \ln\left(\frac{V_f}{V_o}\right) + b \ln\left(\frac{\theta}{\theta_o}\right) \tag{6}$$

In this equation f_o is the friction coefficient at a reference sliding rate V_0, V_f is the sliding velocity, a is a dimensionless friction parameter measuring the strength of the direct velocity dependency, b is a dimensionless coefficient measuring the strength of the state dependence (see Figure 1B), θ is a state variable (that can be interpreted as the average age of asperity on the fault) and θ_0 is the state variable at V_0. In this work, we use the aging law for the evolution of the state (Dieterich, 1979):

$$\frac{\partial \theta}{\partial t} = 1 - \frac{V_f \theta}{d_c} \tag{7}$$

where d_c is the state evolution distance. Our approach to solving for the sliding rate on the fault is as follows: 1) solve the equations governing deformation of the poro-elastic solid for the shear stress on the fault (see Equation 4), 2) set the result to the Coulomb condition (see Equation 5 combined with Equation 6 and Equation 7) and 3) solve for the fault slip rate V_f.

The fluid pressure equation is obtained by combining mass balance of the fluid with Darcy's law. This equation can be written as

$$\beta \frac{\partial P_e}{\partial t} = \nabla . \left(\frac{k}{\eta_f} \nabla P_e \right) - \alpha \nabla . V + S \tag{8}$$

where P_e the fluid pressure in excess of hydrostatic (i.e., $P_e = P_f - \rho_f g z$), β is the effective bulk compressibility (which subsumes the porosity, fluid compressibility, solid compressibility, etc.), ∇ is the gradient operator, k the permeability (considered to vary as a

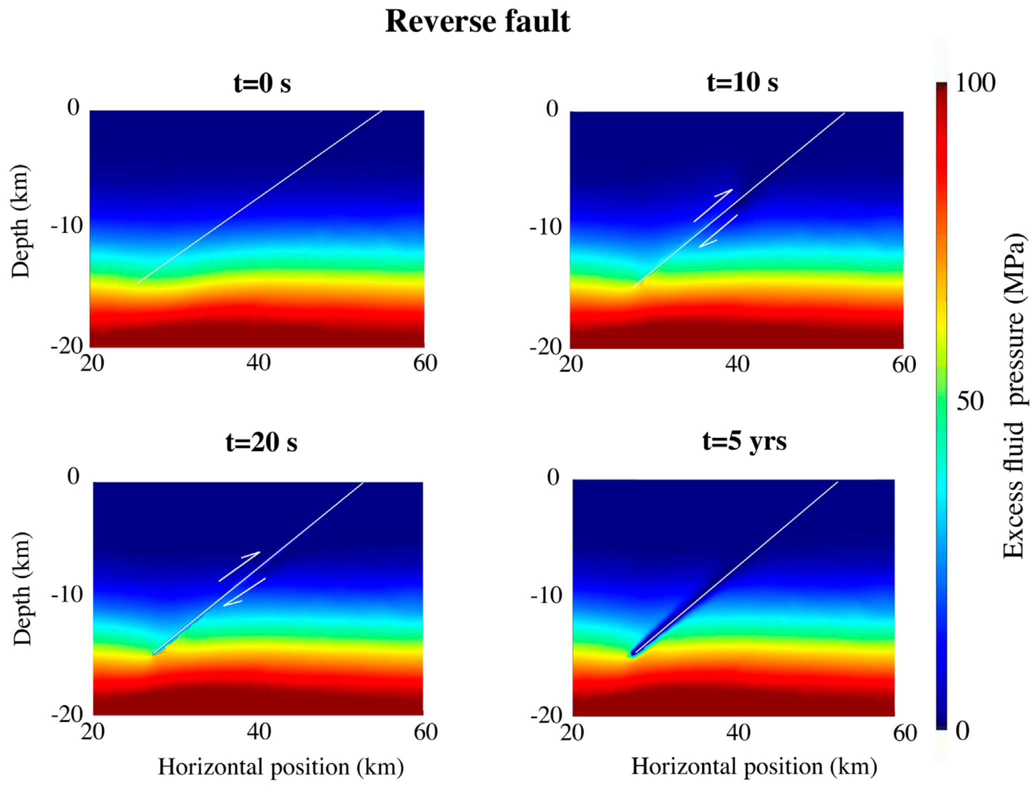

FIGURE 7
Snapshots of the fluid overpressure at different times shortly before, during, and after a large mainshock on a reverse fault with a preexisting fluid overpressure due to fluid production ($S_0 = 10^{-13}$ s^{-1}). Only the part of the model close to the fault (40 km wide and 20 km deep) is shown. The white line in each panel indicates the fault plane.

function of sliding rate and depth, as outlined below), η_f is the viscosity of the fluid, α is Biot's coefficient, V are velocities of the solid and S is a fluid pressure source term (with units (kg H_2O)/[(kg rock)/s] that varies of a function of space (see below). This equation states that variations in fluid pressures occur in response to three effects: porous flow (term 1 on the right-hand side of Equation 8), volumetric deformation of the poro-elastic solid (term 2) and fluid production (term 3).

Fluid overpressures are introduced into the model by considering a fluid source in the crust that increases exponentially with depth:

$$S = S_0\left(1 - \exp\left(\frac{-|z|}{\gamma}\right)\right) \tag{9}$$

where z the depth, S_0 the maximum fluid production rate [(kg H_2O)/(kg rock)/s], and γ is a length scale. This source could represent fluid pressure production by metamorphic devolatisation reactions (Connolly, 1997) or by viscous compaction (Walder and Nur, 1984). The parameters in this equation are chosen in order to obtain a moderate overpressure (amounting to about 65% of the lithostatic pressure for the reverse fault and 45% for the normal fault) close to the base of the fault by the time it ruptures. Similar or greater degrees of overpressure have been estimated in numerous independent studies (e.g., see Sibson et al., 1988; Cox, 2005; Suppe, 2014).

Regarding the crust permeability, we have taken the empirical relation established by Manning and Ingebritsen (1999):

$$\log(k_b) = -14 - 3.2\log(|z|) \tag{10}$$

where z is the depth (in km). The fault permeability is known to change drastically over the duration of the seismic cycle (Miller, 1997). Rapid sliding during an earthquake can produce an extremely high permeability due to fracturing and dilatancy (Cox and Munroe, 2016; Heap and Kennedy, 2016; Im et al., 2019; Ishibashi et al., 2018; Lamur et al., 2017; Sibson, 1986) whereas after an earthquake compaction and mineral precipitation act to reduce permeability (Renard et al., 2000; Tenthorey et al., 2003). We capture these mechanisms using the following heuristic evolution equations

$$\begin{aligned} \frac{\partial k_f}{\partial t} &= \frac{k_{max} - k_f}{T_S} \quad \text{if } V_f \geq V_c \\ \frac{\partial k_f}{\partial t} &= \frac{-k_f}{T_H} \quad \text{if } V_f < V_c \end{aligned} \tag{11}$$

where k_f is the permeability on the fault, k_{max} corresponds to the maximum fault permeability during an earthquake, V_f the fault velocity, V_c is a critical sliding velocity and T_S and T_H are characteristic time scales for the permeability to increase (due to fracturing) and decrease (by healing), respectively. The first equation accounts for an increase in permeability once the slip rate exceeds V_c, while the second equation describes the exponential decay of permeability once rapid sliding has terminated (see Figure 2).

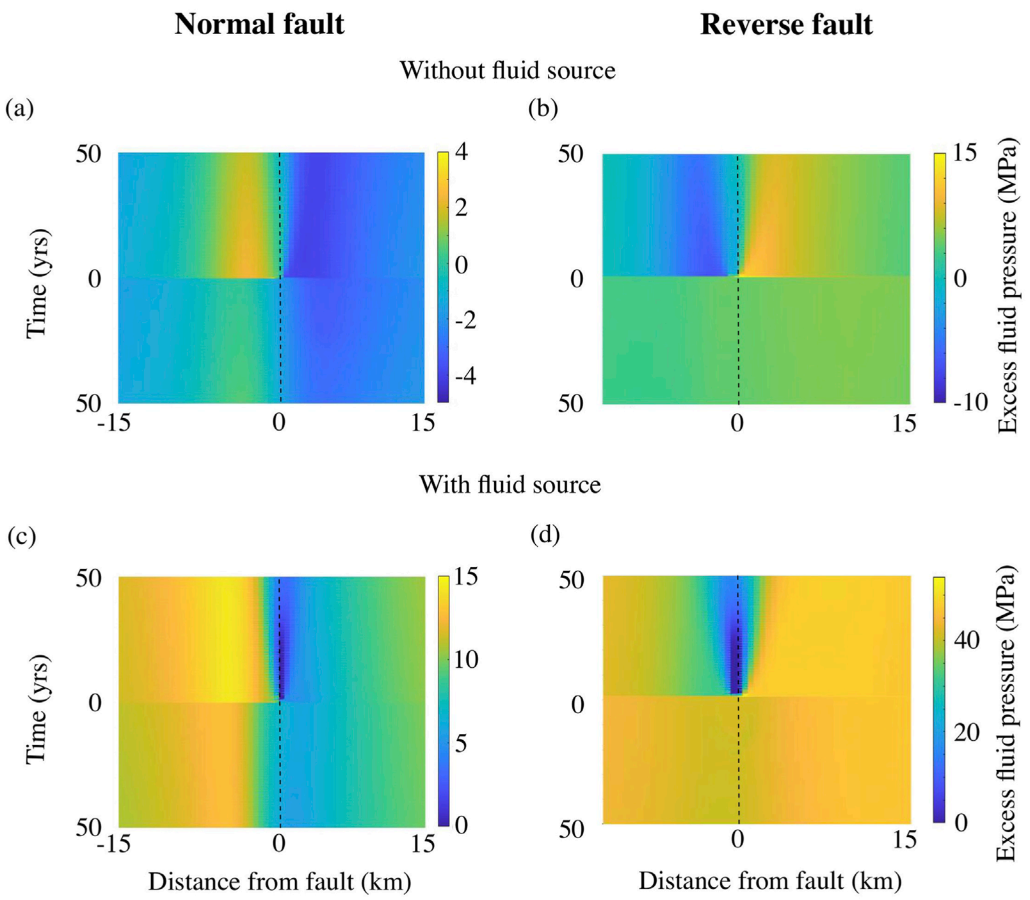

FIGURE 8
Excess fluid pressure at 12.5 km depth several years before and after earthquakes on normal **(A, C)** and reverse **(B, D)** faults. The two upper panels **(A, B)** are results from simulations without a fluid source, whereas the lower panels **(C, D)** are from simulations that included a fluid source. The dashed black lines indicate the fault position. Times are relative to the onset of rupture.

The parameters appearing in these equations are poorly constrained owing to the complexity of the governing processes and the difficulty of obtaining measurements at the relevant spatial and temporal scales. The most important parameter is undoubtedly k_{max}, which controls fluid redistribution during and immediately following earthquakes. Miller et al. (2004) estimated the fault zone permeability to be 4×10^{-11} m^2 immediately following the M6 Colfiorito earthquake sequence of 1997 in central Italy. Noir et al. (1997) inferred a higher fault zone permeability of 10^{-8} m^2 for the Dobi earthquake sequence in Afar in 1989. Due to large uncertainties in k_{max}, we investigate a range of values extending from 10^{-8} to 10^{-10}m^2. For the evolution time scales, we take 1 s for T_S and 2 years for T_H. This latter value is within the range suggested by healing observed on natural faults (Xue et al., 2013). For injection-induced seismicity, the slip is considered seismic if the slip velocity is between 0.1 mm/s and 0.1 m/s (McClure and Horne, 2011; McClure, 2015; Gischig, 2015). Therefore, we take 1 mm/s for the critical sliding velocity (V_c) that controls the transition between a permeability increase and decrease. We note that a similar though different evolution equation for the fault zone permeability was proposed by Zhu et al. (2020). However, whereas we assume that there is a clear distinction between that the permeability changes linked to fracturing and healing (i.e., they are separated in time by a threshold condition), Zhu et al. (2020) consider that the permeability evolution reflects competition between fracture are healing. We also note that in our study (as in that by Zhu et al., 2020), changes in volume linked to sliding are neglected (Segall and Rice, 1995). This is probably a reasonable assumption for a mature fault, but is unlikely to be acceptable during initial fracture development when plastic volume changes are expected to be significant. The total permeability is computed as

$$k = k_b + k_f. \tag{12}$$

Note that k_b appearing in Equation 12 is computed from Equation 10 while k_f is calculated from Equation 11.

The above system of partial differential equations is solved for velocities and fluid pressure using the continuous Galerkin Finite Element method employing 7-node triangles and 7 integration points (Simpson, 2017). We use an unstructured mesh that permits local refinement adjacent to the fault, where the node spacing is ~70 m. Adaptive time stepping is used to transition between the interseismic period (where time steps are on the order

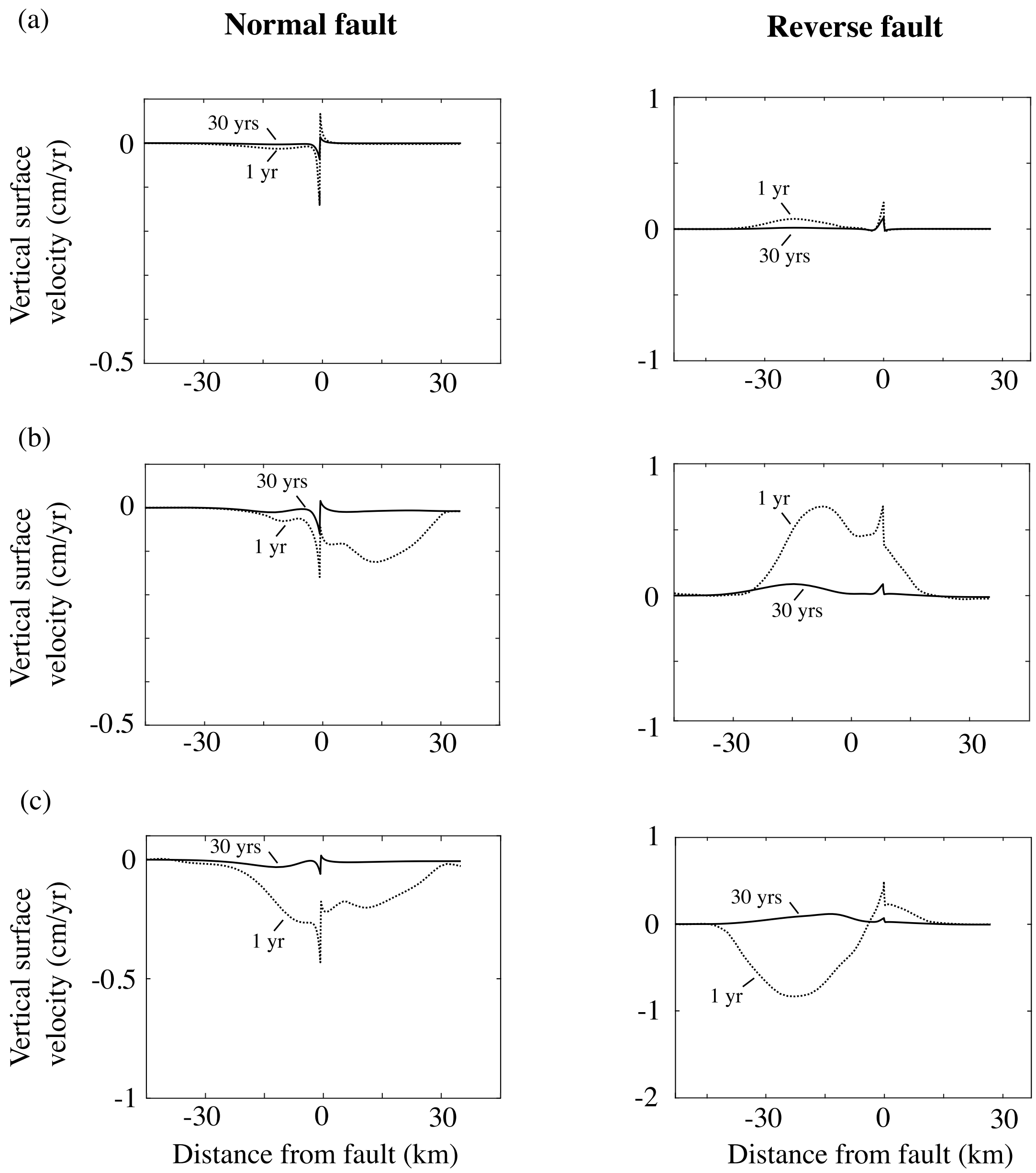

FIGURE 9
Vertical velocities at the surface (with the background velocity removed) following ruptures on normal (left) and reverse (right) faults with different fluid pressure regimes and $K_{max} = 10^{-8} m^2$. Times are relative to the onset of rupture. Three simulations are illustrated: fully drained **(A)**, no pre-rupture fluid overpressure **(B)** and with a pre-rupture fluid overpressure, resulting from a finite fluid source **(C)**.

of 1 year) and times when rupture occurs (where time steps are on the order of 1 μs). To obtain it, we divide an assumed maximum permitted amount of slip during a time step by the maximum calculated fault velocity.

Boundary conditions employed for the numerical calculations are illustrated in Figure 3. We assume that the vertical effective stress is initially given by

$$\sigma_v = \rho(1-\lambda)gz \tag{13}$$

where λ is the pore pressure parameter for hydrostatic conditions ($=0.37 \approx \rho_f/\rho$). The horizontal effective stress is initially assumed to be given by

$$\sigma_h = \begin{cases} R\sigma_v & \text{where} \quad z > -15\text{km} \\ \sigma_v & \text{where} \quad z \leq -15\text{km} \end{cases} \tag{14}$$

where

$$R = \begin{cases} \dfrac{\sqrt{f_0^2+1}-f_0}{\sqrt{f_0^2+1}+f_0} & -\text{extension} \\ \dfrac{\sqrt{f_0^2+1}+f_0}{\sqrt{f_0^2+1}-f_0} & -\text{convergence} \end{cases} \tag{15}$$

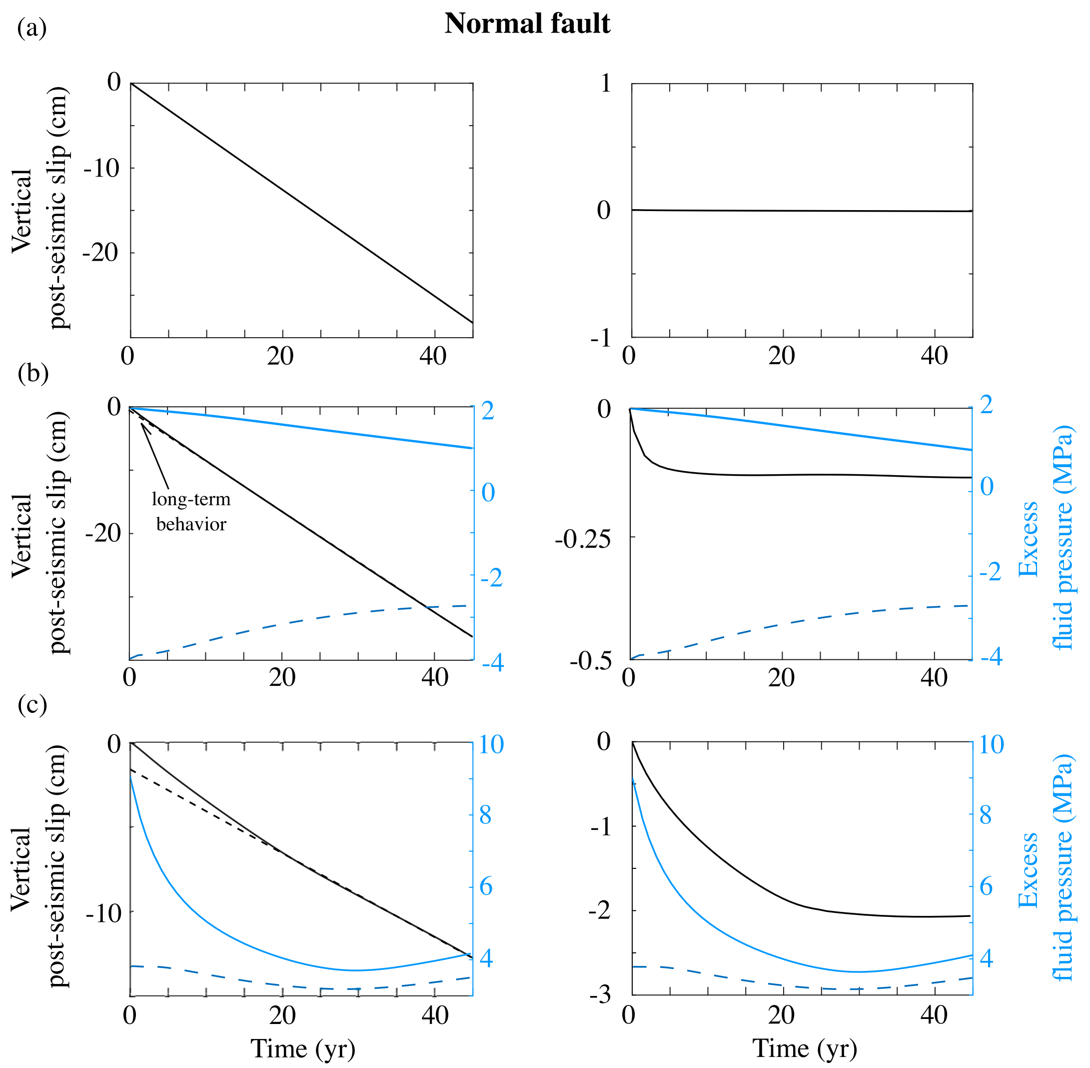

FIGURE 10
Vertical surface displacements in the hanging wall (–10 km from the fault, see Figure 1) and excess fluid pressure at 12.5 km depth and ± 2 km from the fault (i.e., light blue curve for the hanging-wall block and dash dark blue curve for the footwall block) for the time interval immediately following an earthquake (time = 0) on a normal fault with $K_{max} = 10^{-8} m^2$. Results from three different simulations are shown: fully drained **(A)**, no pre-rupture fluid overpressure **(B)** and with a preexisting fluid overpressure **(C)**. The plots on the left show total surface displacements, whereas those on the right have a linear trend removed. The linear trend is indicated as dashed lines in panels on the left, except in **(A)** where the linear trend is the solid line.

where f_0 the reference friction coefficient. We combine Equations 13–15 and assume zero initial shear stress (i.e., σ_{xz}) and zero initial excess pore pressure, which together defines the initial stress state.

3 Results

We seek to understand how coseismic and post-seismic drainage of an overpressured fault zone influences the pressure and displacement fields following ruptures on normal and reverse faults. For comparison we compute results with no fluid pressure variations (i.e., fully drained), which might refer to a system with a very high permeability. In addition, we present results with no pre-rupture fluid overpressure, so that all poroelastic effects are induced by coseismic volumetric strain. We focus mainly on fluid pressure variations and vertical displacements or velocities at the surface.

Figure 4 illustrates the mean slip on normal and reverse faults based on three models: fully drained, without overpressure, and with overpressure at the onset of rupture. For the normal fault, the inter-seismic periods are approximately equivalent. In this case, because the earthquakes nucleate around 6–7 km below the surface, the influence of the fluid source (greatest near the base of the fault) is secondary on the earthquake recurrence. For reverse faults, where nucleation occurs at greater depths (see Supplementary Figure S1), we find that for simulations with overpressure at the onset of the fault slip, the inter-seismic period and co-seismic slip are reduced compared to others simulations, consistent with many previous studies (Kozdon and Dunham, 2013; Lapusta and Rice, 2003; Liu et al., 2005; Marguin and Simpson, 2023).

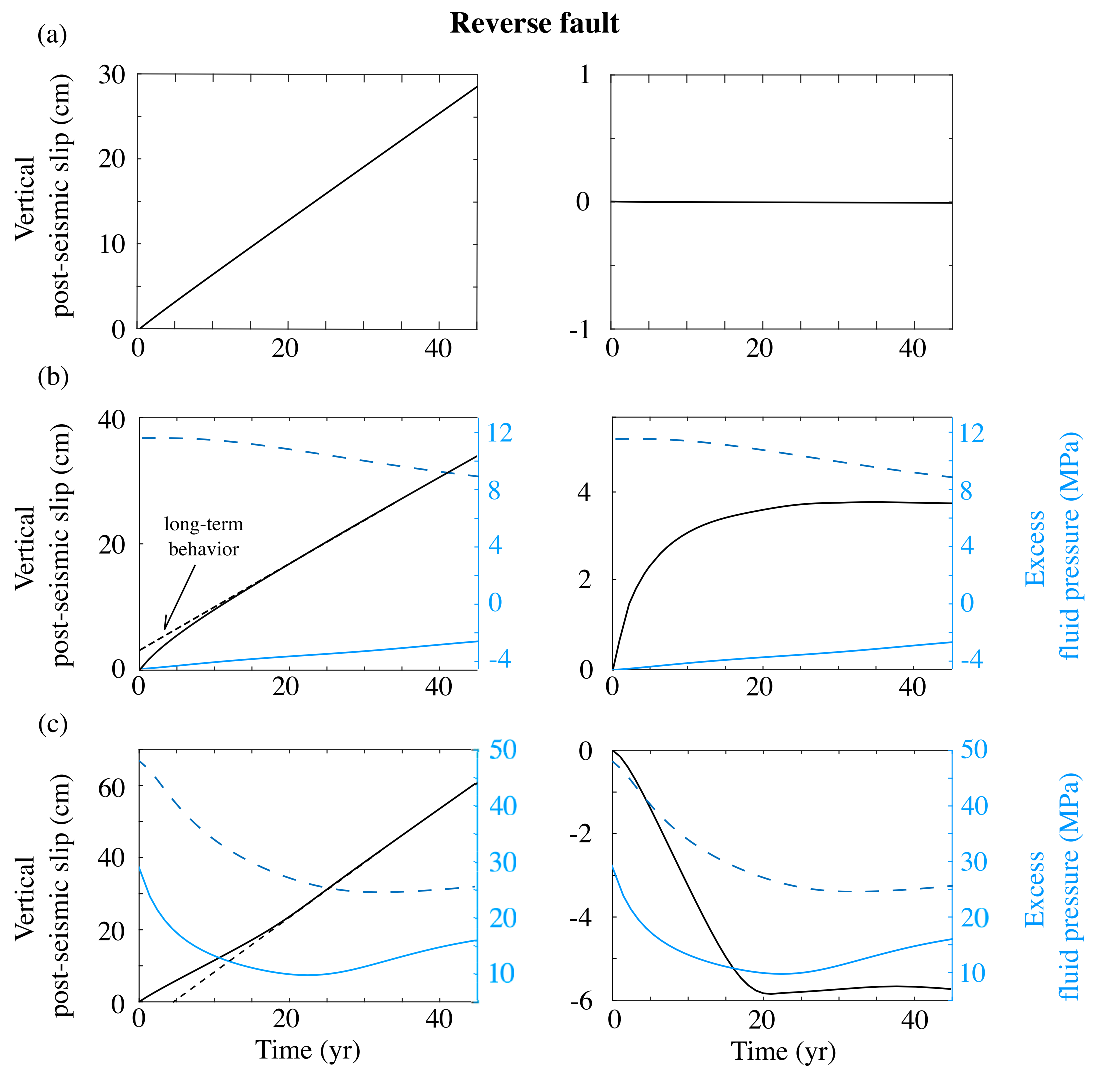

FIGURE 11
Vertical surface displacements in the hanging wall (–10 km from the fault, see Figure 1) and excess fluid pressure at 12.5 km depth and ± 2 km from the fault (i.e., light blue curve for the hanging-wall block and dashed dark blue curve for the footwall block) for the time interval immediately following an earthquake (time = 0) on a reverse fault with $K_{max} = 10^{-8} m^2$. Results from three different simulations are shown: fully drained **(A)**, no pre-rupture fluid overpressure **(B)** and with a preexisting fluid overpressure **(C)**. The plots on the left show total surface displacements, whereas those on the right have a linear trend removed. The linear trend is indicated as dashed lines in panels on the left, except in **(A)** where the linear trend is the solid line.

Figure 5 shows excess fluid pressures shortly before, during and immediately after ruptures on normal and reverse faults in partially-drained simulations without a fluid source. In both cases, fluid pressure variations are directly linked with changes in coseismic volumetric strain, with compressional zones generating positive fluid pressure anomalies and extensional regions leading to reduction in fluid pressures. The fluid pressure anomalies associated with the normal fault rupture are opposite in sign to those related to the reverse rupture and they are a factor of several times smaller because the ruptures are smaller in extension, due to the less compressive stress state and lower shear stress level (see also Supplementary Figure S1). Although the coseismic fluid pressure anomalies dissipate somewhat after rupture, they continue to persist during the interseismic period, especially near the base of faults due to relatively low permeabilities at depth.

Figures 6, 7 illustrate fluid pressures associated with ruptures on normal and reverse faults in simulations with a long term fluid source at depth. In both cases, the bases of the faults are significantly overpressured at the onset of ruptures. During ruptures, fluid pressure variations are mostly induced by changes in coseismic volumetric strain, as they were previously (i.e., see Figure 5 and also Figures 8A, B). Although the faults experience a large coseismic increase in permeability on the faults, there is insufficient time during ruptures to enable significant drainage of the pre-rupture fluid pressure anomalies. However, large decreases in excess fluid pressures are observed close to the faults in the few years following ruptures (see also Figures 8C, D), which results from fluid flow up the fault. Efficient fluid pressure drainage is favoured by large increases in coseismic permeability and relatively long permeability healing times (i.e., large k_{max} and T_H).

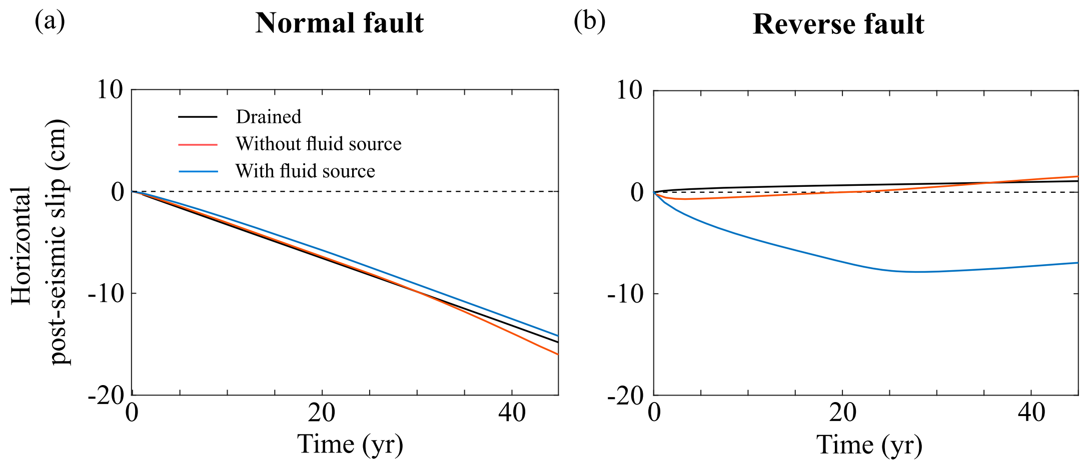

FIGURE 12
Horizontal surface displacements in the hanging wall (–10 km from the fault, see Figure 1) for the time interval immediately following an earthquake (time = 0), with $K_{max} = 10^{-8} m^2$, on a normal **(A)** and reverse **(B)** fault encompassing 3 simulations: fully drained (black curve), no pre-rupture fluid overpressure (red curve) and with a pre-rupture fluid overpressure (blue curve).

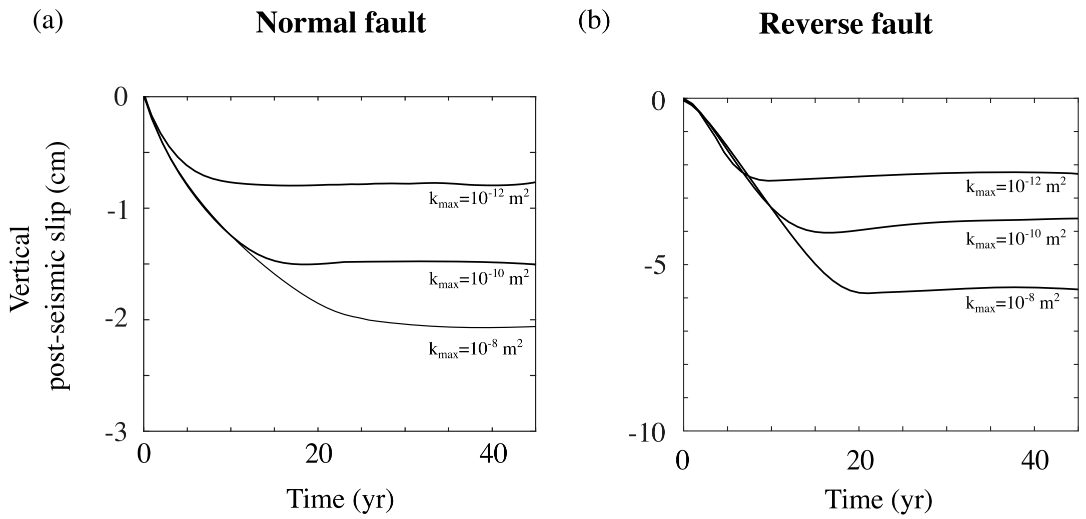

FIGURE 13
Vertical surface displacements in the hanging wall (–10 km from the fault, see Figure 1) versus time following ruptures on normal **(A)** and reverse **(B)** faults from simulations with long term fluid production, computed with different coseismic fault permeabilities k_{max}. Long-term deformation has been removed (see dashed black curve in Figures 10, 11).

Figure 9 illustrates vertical velocities at the surface (with the background velocity removed) following ruptures on normal and reverse faults for the various fluid pressure scenarios. For the fully drained cases (Figure 9A), one observes only minor differences in velocities following rupture, which are localised close to the fault trace and largely independent of time. For simulations that include coseismic fluid pressure variations but without a fluid source, the surface velocity depends sensitively on the loading regime, with post-seismic subsidence in the case of normal faulting and postseismic uplift in the case of reverse faulting (Figure 9B). These effects are directly linked to the relaxation of coseismic fluid pressure anomalies generated close to the surface. For the simulations that included a finite fluid source, one observes post-seismic subsidence for both faulting regimes. In such cases, the surface subsidence is the result of drainage of a deep fluid pressure anomaly permitted by the permeability increase during rupture. The time scales of the post-seismic velocity variations at the surface in all models are controlled by the permeability structure of the crust and fault zone following rupture, since it controls how rapidly fluid pressure anomalies can be equilibrated. For the permeability parameters used in the simulations, the poroelastic response lasts a few years and is largely complete after about 1-2 decades.

Figures 10, 11 shows similar results but in this case plotted in terms of vertical displacements and fluid pressures of single points versus time. Several aspects are noteworthy. First, in fully-drained models, displacements of the hangingwall blocks are linear in time (Figures 10A, 11A), whereas in all other models they are nonlinear, due to variations in fluid pressure. Second, in partially-drained models without a fluid pressure anomaly prior to rupture, the variations in displacement and fluid pressure are opposite for normal and reverse faulting (Figures 10B, 11B). This is because the fluid pressure anomalies result from variations in coseismic volumetric strain, which depend directly on the faulting style. Third, in models where faults are overpressured prior to rupture, both the fluid pressure and surface displacement responses are independent of fault style and are dominated by drainage of the pre-rupture fluid pressure anomaly. For the models investigated, the magnitude of the poroelastic response is significantly larger (by a factor of about 10) that in models where fluid pressure variations result solely from faulting.

Figure 12 shows horizontal displacements of single points versus time following ruptures on normal and reverse faults for the same fluid pressure scenarios. In the case of a normal fault (see Figure 12A), we found that the horizontal displacement at the surface following an earthquake is linear and decreases in time, indicating that the hangingwall block moves to the left (i.e., in the extensional direction, see Figure 1B). For this fault type, there is little difference in horizontal displacement between the three model scenarios (fully drained, without fluid overpressure before rupture, and with fluid overpressure before rupture). Thus, in this case, horizontal displacements are insensitive to postseismic drainage of fluid pressure anomalies. In the case of reverse faulting, the hangingwall block is expected to move in the direction of compression following an earthquake, as is observed in the fully drained model (see black curve in Figure 12B). However, in the model where the fault was overpressured at the time of rupture, the hangwall block experiences a phase lasting ~20 years when it moves in the opposite direction (i.e., it moves towards the left), which is presumably related to relaxation of the fluid pressure anomaly at depth (see blue curve in Figure 12B). A similar though far less pronounced phase of "reversed motion" is observed in the partially drained model with no fluid source (red curve in Figure 12B).

In models where faults are overpressurised at the onset of rupture, the time scale for poroelastic relaxation is dependent on the maximum coseismic permeability k_{max} and the permeability healing time scale T_H. Reducing the maximum coseismic permeability or the healing time scale leads to a faster recovery of permeability after an earthquake, decreasing the duration of poroelastic deformation caused by fault drainage (Figure 13). In addition, we find that the larger the maximum coseismic permeability k_{max}, the greater is the magnitude of poroelastic subsidence (Figure 13).

4 Discussion

Many studies have drawn upon poroelasticity in order to explain transient displacement fields following large earthquakes (e.g., Peltzer et al., 1996; 1998; McCormack et al., 2020; Peña et al., 2022). However in most previous work, the poroelastic effects investigated are linked to the relaxation of pore pressure anomalies created during coseismic slip. Here we focus on a different poroelastic phenonemon that stems from the possibility that faults may already be overpressured at the time of rupture (e.g., see Sibson et al., 1988; Sibson, 1990; Cox, 2005; Curzi et al., 2023). We highlight that drainage from an overpressured fault zone can have an important additional influence on the postseismic displacement field following rupture. Ultimately, our results suggest that the postseismic displacements (especially in the vertical direction) may contain important information concerning the fluid pressure state and permeability structure of faults during and immediately following earthquakes.

In this research we have shown that in situations where faults are overpressurised at the time they rupture, then fluid drainage along a ruptured fault and the resulting fluid pressure decrease may induce a distinct phase of postseismic subsidence, observable at the surface. The time scale and magnitude of this poroelastic subsidence (i.e., above overpressurised faults) depends on the coseismic permeability and on how rapidly the fault permeability recovers following an earthquake, whereas it is independent of the size of an earthquake, since it is driven not by the magnitude of coseismic slip but by the magnitude of fluid pressure relaxation. This relaxation occurs irrespective of the faulting regime and fault geometry and is therefore quite different from the classic coseismic poroelastic response (Segall, 2010) as well as other postseismic effects related to either post-rupture fault slip (e.g., Freed et al., 2017; Guo et al., 2019a; Huang et al., 2017; Shrivastava et al., 2016) or viscous deformation (e.g., Freed and Lin, 2001; Guo et al., 2019b). In addition, whereas the magnitude of pore pressure changes induced by coseismic strain are typically on the order of 1 MPa, the variations resulting from rupture of previously overpressurised fault zones are potentially at least an order of magnitude greater.

Although we have not attempted to apply our models to specific observations, our results might aid in interpreting and understanding some data. For example, Pritchard et al. (2013) observed significant post-seismic subsidence in the weeks following the 2010 Maule earthquake in Chile. They suggest that this subsidence is possibly associated with the release of fluids from hydrothermal systems, facilitated by increased permeability in fault zones, which is consistent with our models (see Figures 10, 11, 13). A similar explanation was proposed to account for anomalous subsidence of the Yellowstone caldera linked to seismicity which began in 1985 (Waite and Smith, 2002). In cases when faults are not significantly overpressured at the time of rupture, we expect a normal poroelastic postseismic geodetic response, similar to that which has been described in previous studies (e.g., Peltzer et al., 1996; 1998; McCormack et al., 2020; Peña et al., 2022). Some studies have noted that the hydrological changes induced by earthquakes that are not well predicted by the coseismic strain field (e.g., Cox et al., 2012; Manga and Rowland, 2009; Wang et al., 2004), which is consistent with our model results when faults are overpressurised. Cox et al. (2012) in particular suggested that groundwater changes and liquefaction associated with the 2011 Darfield earthquake near Christchurch (New Zealand) resulted from rapid fluid release from an overpressured reservoir, which is entirely plausible based on our results. Similar interpretations have been made by Miller et al. (2004) and Terakawa et al. (2010). Other studies have noted significant changes in seismic velocities of the crust surrounding recently ruptured faults (Chaves and Schwartz, 2016; Chiarabba et al., 2022). Large fluid pressure changes resulting from rupture would provide a potential explanation for these transient variations, though other explanations are also possible (Rubinstein and Beroza, 2004).

At this stage, there are several factors that severely limit the predictive capability of our modelling. First, we have somewhat arbitrarily assumed that fluid pressures are generated in the lower part of the crust. Although we think this is plausible, we have not attempted to incorporate specific processes responsible for fluid production (e.g., dehydration reactions) or to quantify whether our fluid production rates are physically reasonable. Having said that, the magnitude of our fluid pressure anomalies at the time of rupture are reasonable in that many studies have reported evidence for significant fluid overpressures at mid-crustal depths (Etheridge et al., 1984; Fisher et al., 1995; Sibson, 2017; Suppe, 2014). Second, we have assumed an ad hoc law describing how the permeability changes over an earthquake cycle. Our equation is physically reasonable but governed by two poorly constrained parameters, the maximum coseismic permeability (k_{max}) and the time scale for permeability recovery (T_H). We have employed a range of values for (k_{max}), accepting that is both poorly known and difficult to directly measure. We have only studied one value for T_H (=2 years), though this is consistent with some research (Xue et al., 2013). Despite these uncertainties, we observe poroelastic response time scales of 1–10 years, which are plausible based on observations (e.g., Manga and Wang, 2015). Third, we have neglected other more widely accepted factors that may be responsible for postseismic deformation, especially post-rupture fault slip (e.g., Freed et al., 2017; Guo et al., 2019a; Shrivastava et al., 2016) and viscous deformation in the lower crust or mantle (e.g., Freed and Lin, 2001; Guo et al., 2019b). We omitted these factors not because we think that they are unimportant, rather because we wanted to be able to clearly identify poroelastic effects. More research is required to evaluate how the poroelastic behaviour identified here operates in a crust with other viscoelastic effects. Interested readers are referred to studies such as Barbot and Fialko (2010) and Dal Zilio and Gerya (2022) who have combined poroelastic behaviour with viscous and/or visco-plastic flow. Finally, we have also neglected dynamic effects (i.e., related to the propagation of seismic waves) that may be be produced by earthquakes and that may also induce various hydrological changes (Maestrelli et al., 2017; Lupi et al., 2013).

5 Conclusion

Our study shows that the poroelastic response to earthquakes on dip-slip faults depends critically on the fluid pressure state in the crust prior to rupture. If the crust is normally pressurised (i.e., with hydrostatic fluid pressures) then pore-pressure variations induced by rupture are entirely controlled by the field of volumetric elastic strain. In this case, the poroelastic response depends on the magnitude of coseismic slip and the faulting style. On the other hand, if the crust is appreciably overpressured at the time of rupture, these effects may be entirely overwhelmed by the overall tendency for drainage and fluid pressure decrease from the overpressured crust. In this case, postseismic subsidence is observed at the surface irrespective of fault style or details of the strain field. The magnitude of this postseismic subsidence could be at least an order of magnitude greater than the classic poroelastic response (i.e., relaxation of pore pressures generated by coseismic elastic volumetric strain). Large postseismic subsidence is favoured by large pre-rupture fluid overpressures, large permeabilities during rupture and slow recovery of the permeability following rupture. The results suggest that postseismic deformation associated with overpressured crust may be distinctly different from that in crust with no long term fluid overpressure.

Data availability statement

The original contributions presented in the study are included in the article/Supplementary Material, further inquiries can be directed to the corresponding author.

Author contributions

VM: Conceptualization, Formal Analysis, Investigation, Methodology, Validation, Visualization, Writing–original draft, Writing–review and editing. GS: Conceptualization, Formal Analysis, Funding acquisition, Investigation, Methodology, Project administration, Supervision, Validation, Writing–original draft, Writing–review and editing, Visualization.

Funding

The author(s) declare that financial support was received for the research, authorship, and/or publication of this article. The Swiss National Science Foundation (project 200021_184626) is thanked for funding.

Conflict of interest

The authors declare that the research was conducted in the absence of any commercial or financial relationships that could be construed as a potential conflict of interest.

Publisher's note

Supplementary material

The Supplementary Material for this article can be found online at: https://www.frontiersin.org/articles/10.3389/feart.2024.1423174/full#supplementary-material

References

Akita, F., and Matsumoto, N. (2004). Hydrological responses induced by the Tokachi-oki earthquake in 2003 at hot spring wells in Hokkaido, Japan. *Geophys. Res. Lett.* 31. doi:10.1029/2004gl020433

Árnadóttir, T., Jónsson, S., Pollitz, F. F., Jiang, W., and Feigl, K. L. (2005). Postseismic deformation following the June 2000 earthquake sequence in the south Iceland seismic zone. *J. Geophys. Res. Solid Earth* 110. doi:10.1029/2005jb003701

Barbot, S., and Fialko, Y. (2010). A unified continuum representation of post-seismic relaxation mechanisms: semi-analytic models of afterslip, poroelastic rebound and viscoelastic flow. *Geophys. J. Int.* 182, 1124–1140. doi:10.1111/j.1365-246x.2010.04678.x

Chaves, E. J., and Schwartz, S. Y. (2016). Monitoring transient changes within overpressured regions of subduction zones using ambient seismic noise. *Sci. Adv.* 2, e1501289. doi:10.1126/sciadv.1501289

Chiarabba, C., De Gori, P., Valoroso, L., Petitta, M., and Carminati, E. (2022). Large extensional earthquakes push-up terrific amount of fluids. *Sci. Rep.* 12, 14597. doi:10.1038/s41598-022-18688-6

Connolly, J. (1997). Devolatilization-generated fluid pressure and deformation-propagated fluid flow during prograde regional metamorphism. *J. Geophys. Res. Solid Earth* 102, 18149–18173. doi:10.1029/97jb00731

Cox, S. C., Rutter, H., Sims, A., Manga, M., Weir, J., Ezzy, T., et al. (2012). Hydrological effects of the mw 7.1 Darfield (canterbury) earthquake, 4 september 2010, New Zealand. *N. Z. J. Geol. Geophys.* 55, 231–247. doi:10.1080/00288306.2012.680474

Cox, S. C., van Ballegooy, S., Rutter, H. K., Harte, D. S., Holden, C., Gulley, A. K., et al. (2021). Can artesian groundwater and earthquake-induced aquifer leakage exacerbate the manifestation of liquefaction? *Eng. Geol.* 281, 105982. doi:10.1016/j.enggeo.2020.105982

Cox, S. F. (2005) "Coupling between deformation, fluid pressures, and fluid flow in ore-producing hydrothermal systems at depth in the crust," in *One hundredth anniversary*, Volume. Littleton, USA: Society of Economic Geologists. doi:10.5382/av100.04

Cox, S. F., and Munroe, S. M. (2016). Breccia formation by particle fluidization in fault zones: implications for transitory, rupture-controlled fluid flow regimes in hydrothermal systems. *Am. J. Sci.* 316, 241–278. doi:10.2475/03.2016.02

Curzi, M., Cipriani, A., Aldega, L., Billi, A., Carminati, E., Van der Lelij, R., et al. (2023). Architecture and permeability structure of the sibillini mts. thrust and influence upon recent, extension-related seismicity in the central apennines (Italy) through fault-valve behavior. *GSA Bull.* 136, 3–26. doi:10.1130/b36616.1

Dal Zilio, L., and Gerya, T. (2022). Subduction earthquake cycles controlled by episodic fluid pressure cycling. *Lithos* 426, 106800. doi:10.1016/j.lithos.2022.106800

Dieterich, J. H. (1979). Modeling of rock friction: 1. experimental results and constitutive equations. *J. Geophys. Res. Solid Earth* 84, 2161–2168. doi:10.1029/jb084ib05p02161

Doglioni, C., Barba, S., Carminati, E., and Riguzzi, F. (2014). Fault on–off versus coseismic fluids reaction. *Geosci. Front.* 5, 767–780. doi:10.1016/j.gsf.2013.08.004

Etheridge, M. A., Wall, V., Cox, S. F., and Vernon, R. (1984). High fluid pressures during regional metamorphism and deformation: implications for mass transport and deformation mechanisms. *J. Geophys. Res. Solid Earth* 89, 4344–4358. doi:10.1029/jb089ib06p04344

Fialko, Y. (2004). Evidence of fluid-filled upper crust from observations of postseismic deformation due to the 1992 M_w7.3 Landers earthquake. *J. Geophys. Res. Solid Earth* 109. doi:10.1029/2004jb002985

Fisher, D. M., Brantley, S. L., Everett, M., and Dzvonik, J. (1995). Cyclic fluid flow through a regionally extensive fracture network within the Kodiak accretionary prism. *J. Geophys. Res. Solid Earth* 100, 12881–12894. doi:10.1029/94jb02816

Freed, A. M., Hashima, A., Becker, T. W., Okaya, D. A., Sato, H., and Hatanaka, Y. (2017). Resolving depth-dependent subduction zone viscosity and afterslip from postseismic displacements following the 2011 tohoku-oki, Japan earthquake. *Earth Planet. Sci. Lett.* 459, 279–290. doi:10.1016/j.epsl.2016.11.040

Freed, A. M., and Lin, J. (2001). Delayed triggering of the 1999 Hector Mine earthquake by viscoelastic stress transfer. *Nature* 411, 180–183. doi:10.1038/35075548

Gischig, V. S. (2015). Rupture propagation behavior and the largest possible earthquake induced by fluid injection into deep reservoirs. *Geophys. Res. Lett.* 42, 7420–7428. doi:10.1002/2015gl065072

Guo, R., Zheng, Y., Xu, J., and Jiang, Z. (2019a). Seismic and aseismic fault slip associated with the 2017 Mw 8.2 Chiapas, Mexico, earthquake sequence. *Seismol. Res. Lett.* 90, 1111–1120. doi:10.1785/0220180262

Guo, R., Zheng, Y., Xu, J., and Riaz, M. S. (2019b). Transient viscosity and afterslip of the 2015 Mw 8.3 Illapel, Chile, earthquake. *Bull. Seismol. Soc. Am.* 109, 2567–2581. doi:10.1785/0120190114

Heap, M. J., and Kennedy, B. M. (2016). Exploring the scale-dependent permeability of fractured andesite. *Earth Planet. Sci. Lett.* 447, 139–150. doi:10.1016/j.epsl.2016.05.004

Huang, M.-H., Fielding, E. J., Liang, C., Milillo, P., Bekaert, D., Dreger, D., et al. (2017). Coseismic deformation and triggered landslides of the 2016 *w* 6.2 Amatrice earthquake in Italy. *Geophys. Res. Lett.* 44, 1266–1274. doi:10.1002/2016gl071687

Hughes, K. L., Masterlark, T., and Mooney, W. D. (2010). Poroelastic stress-triggering of the 2005 M8. 7 nias earthquake by the 2004 M9.2 sumatra–andaman earthquake. *Earth Planet. Sci. Lett.* 293, 289–299. doi:10.1016/j.epsl.2010.02.043

Im, K., Elsworth, D., and Wang, C. (2019). Cyclic permeability evolution during repose then reactivation of fractures and faults. *J. Geophys. Res. Solid Earth* 124, 4492–4506. doi:10.1029/2019jb017309

Ishibashi, T., Elsworth, D., Fang, Y., Riviere, J., Madara, B., Asanuma, H., et al. (2018). Friction-stability-permeability evolution of a fracture in granite. *Water Resour. Res.* 54, 9901–9918. doi:10.1029/2018wr022598

Jónsson, S., Segall, P., Pedersen, R., and Björnsson, G. (2003). Post-earthquake ground movements correlated to pore-pressure transients. *Nature* 424, 179–183. doi:10.1038/nature01776

Koizumi, N., Kitagawa, Y., Matsumoto, N., Takahashi, M., Sato, T., Kamigaichi, O., et al. (2004). Preseismic groundwater level changes induced by crustal deformations related to earthquake swarms off the east coast of Izu Peninsula, Japan. *Geophys. Res. Lett.* 31. doi:10.1029/2004gl019557

Kozdon, J. E., and Dunham, E. M. (2013). Rupture to the trench: dynamic rupture simulations of the 11 March 2011 Tohoku earthquake. *Bull. Seismol. Soc. Am.* 103, 1275–1289. doi:10.1785/0120120136

Lamur, A., Kendrick, J., Eggertsson, G., Wall, R., Ashworth, J., and Lavallée, Y. (2017). The permeability of fractured rocks in pressurised volcanic and geothermal systems. *Sci. Rep.* 7, 6173. doi:10.1038/s41598-017-05460-4

Lapusta, N., and Rice, J. R. (2003). Nucleation and early seismic propagation of small and large events in a crustal earthquake model. *J. Geophys. Res. Solid Earth* 108. doi:10.1029/2001jb000793

Liu, S.-F., Nummedal, D., Yin, P.-G., and Luo, H.-J. (2005). Linkage of Sevier thrusting episodes and Late Cretaceous foreland basin megasequences across southern Wyoming (USA). *Basin Res.* 17, 487–506. doi:10.1111/j.1365-2117.2005.00277.x

Lupi, M., Saenger, E. H., Fuchs, F., and Miller, S. A. (2013). Lusi mud eruption triggered by geometric focusing of seismic waves. *Nat. Geosci.* 6, 642–646. doi:10.1038/ngeo1884

Maestrelli, D., Bonini, M., Delle Donne, D., Manga, M., Piccardi, L., and Sani, F. (2017). Dynamic triggering of mud volcano eruptions during the 2016–2017 Central Italy seismic sequence. *J. Geophys. Res. Solid Earth* 122, 9149–9165. doi:10.1002/2017jb014777

Manga, M., and Rowland, J. C. (2009). Response of alum rock springs to the October 30, 2007 Alum rock earthquake and implications for the origin of increased discharge after earthquakes. *Geofluids* 9, 237–250. doi:10.1111/j.1468-8123.2009.00250.x

Manga, M., and Wang, C. (2015). Earthquake hydrology. *Treatise Geophys.*, 305–328. doi:10.1016/b978-0-444-53802-4.00082-8

Manning, C. E., and Ingebritsen, S. E. (1999). Permeability of the continental crust: implications of geothermal data and metamorphic systems. *Rev. Geophys.* 37, 127–150. doi:10.1029/1998rg900002

Marguin, V., and Simpson, G. (2023). Influence of fluids on earthquakes based on numerical modeling. *J. Geophys. Res. Solid Earth* 128, e2022JB025132. doi:10.1029/2022jb025132

Marone, C. (1998). The effect of loading rate on static friction and the rate of fault healing during the earthquake cycle. *Nature* 391, 69–72. doi:10.1038/34157

McClure, M. W. (2015). Generation of large postinjection-induced seismic events by backflow from dead-end faults and fractures. *Geophys. Res. Lett.* 42, 6647–6654. doi:10.1002/2015gl065028

McClure, M. W., and Horne, R. N. (2011). Investigation of injection-induced seismicity using a coupled fluid flow and rate/state friction model. *Geophysics* 76, WC181–WC198. doi:10.1190/geo2011-0064.1

McCormack, K., Hesse, M. A., Dixon, T., and Malservisi, R. (2020). Modeling the contribution of poroelastic deformation to postseismic geodetic signals. *Geophys. Res. Lett.* 47, e2020GL086945. doi:10.1029/2020gl086945

Miller, S. A. (1997). *The behavior of 3-Dimensional fluid-controlled earthquake model: applications and implications.* ETH Zurich.

Miller, S. A., Collettini, C., Chiaraluce, L., Cocco, M., Barchi, M., and Kaus, B. J. (2004). Aftershocks driven by a high-pressure CO2 source at depth. *Nature* 427, 724–727. doi:10.1038/nature02251

Muir-Wood, R., and King, G. C. (1993). Hydrological signatures of earthquake strain. *J. Geophys. Res. Solid Earth* 98, 22035–22068. doi:10.1029/93jb02219

Noir, J., Jacques, E., Bekri, S., Adler, P., Tapponnier, P., and King, G. (1997). Fluid flow triggered migration of events in the 1989 Dobi earthquake sequence of Central Afar. *Geophys. Res. Lett.* 24, 2335–2338. doi:10.1029/97gl02182

Norton, D. L. (1984). Theory of hydrothermal systems. *Annu. Rev. Earth Planet. Sci.* 12, 155–177. doi:10.1146/annurev.earth.12.1.155

Peltzer, G., Rosen, P., Rogez, F., and Hudnut, K. (1996). Postseismic rebound in fault step-overs caused by pore fluid flow. *Science* 273, 1202–1204. doi:10.1126/science.273.5279.1202

Peltzer, G., Rosen, P., Rogez, F., and Hudnut, K. (1998). Poroelastic rebound along the Landers 1992 earthquake surface rupture. *J. Geophys. Res. Solid Earth* 103, 30131–30145. doi:10.1029/98jb02302

Peña, C., Heidbach, O., Moreno, M., Bedford, J., Ziegler, M., Tassara, A., et al. (2020). Impact of power-law rheology on the viscoelastic relaxation pattern and afterslip distribution following the 2010 Mw 8.8 Maule earthquake. *Earth Planet. Sci. Lett.* 542, 116292. doi:10.1016/j.epsl.2020.116292

Peña, C., Metzger, S., Heidbach, O., Bedford, J., Bookhagen, B., Moreno, M., et al. (2022). Role of poroelasticity during the early postseismic deformation of the 2010 Maule megathrust earthquake. *Geophys. Res. Lett.* 49, e2022GL098144. doi:10.1029/2022gl098144

Pritchard, M., Jay, J., Aron, F., Henderson, S., and Lara, L. (2013). Subsidence at southern Andes volcanoes induced by the 2010 Maule, Chile earthquake. *Nat. Geosci.* 6, 632–636. doi:10.1038/ngeo1855

Quilty, E. G., and Roeloffs, E. A. (1997). Water-level changes in response to the 20 December 1994 earthquake near Parkfield, California. *Bull. Seismol. Soc. Am.* 87, 310–317. doi:10.1785/bssa0870020310

Renard, F., Gratier, J.-P., and Jamtveit, B. (2000). Kinetics of crack-sealing, intergranular pressure solution, and compaction around active faults. *J. Struct. Geol.* 22, 1395–1407. doi:10.1016/s0191-8141(00)00064-x

Rubinstein, J. L., and Beroza, G. C. (2004). Evidence for widespread nonlinear strong ground motion in the mw 6.9 Loma Prieta earthquake. *Bull. Seismol. Soc. Am.* 94, 1595–1608. doi:10.1785/012004009

Ruina, A. (1983). Slip instability and state variable friction laws. *J. Geophys. Res. Solid Earth* 88, 10359–10370. doi:10.1029/jb088ib12p10359

Segall, P. (2010). *Earthquake and volcano deformation*. Princeton University Press.

Segall, P., and Rice, J. R. (1995). Dilatancy, compaction, and slip instability of a fluid-infiltrated fault. *J. Geophys. Res. Solid Earth* 100, 22155–22171. doi:10.1029/95jb02403

Shrivastava, M. N., González, G., Moreno, M., Chlieh, M., Salazar, P., Reddy, C., et al. (2016). Coseismic slip and afterslip of the 2015 *w* 8.3 Illapel (Chile) earthquake determined from continuous GPS data. *Geophys. Res. Lett.* 43, 10–710. doi:10.1002/2016gl070684

Sibson, R. H. (1986). Rupture interaction with fault jogs. *Earthq. Source Mech.* 37, 157–167. doi:10.1029/gm037p0157

Sibson, R. H. (1990) *Conditions for fault-valve behaviour*, 54. London, UK: Geological Society, London, Special Publications, 15–28.

Sibson, R. H. (2017). Tensile overpressure compartments on low-angle thrust faults. *Earth, Planets Space* 69, 113–115. doi:10.1186/s40623-017-0699-y

Sibson, R. H., Robert, F., and Poulsen, K. H. (1988). High-angle reverse faults, fluid-pressure cycling, and mesothermal gold-quartz deposits. *Geology* 16, 551–555. doi:10.1130/0091-7613(1988)016<0551:harffp>2.3.co;2

Simpson, G. (2017). *Practical finite element modeling in earth science using matlab*. John Wiley and Sons.

Suppe, J. (2014). Fluid overpressures and strength of the sedimentary upper crust. *J. Struct. Geol.* 69, 481–492. doi:10.1016/j.jsg.2014.07.009

Tenthorey, E., Cox, S. F., and Todd, H. F. (2003). Evolution of strength recovery and permeability during fluid–rock reaction in experimental fault zones. *Earth Planet. Sci. Lett.* 206, 161–172. doi:10.1016/s0012-821x(02)01082-8

Terakawa, T., Zoporowski, A., Galvan, B., and Miller, S. A. (2010). High-pressure fluid at hypocentral depths in the l'aquila region inferred from earthquake focal mechanisms. *Geology* 38, 995–998. doi:10.1130/g31457.1

Waite, G. P., and Smith, R. B. (2002). Seismic evidence for fluid migration accompanying subsidence of the yellowstone caldera. *J. Geophys. Res. Solid Earth* 107. doi:10.1029/2001jb000586

Walder, J., and Nur, A. (1984). Porosity reduction and crustal pore pressure development. *J. Geophys. Res. Solid Earth* 89, 11539–11548. doi:10.1029/jb089ib13p11539

Wang, C.-Y., Cheng, L.-H., Chin, C.-V., and Yu, S.-B. (2001). Coseismic hydrologic response of an alluvial fan to the 1999 Chi-Chi earthquake, Taiwan. *Geology* 29, 831–834. doi:10.1130/0091-7613(2001)029<0831:chroaa>2.0.co;2

Wang, C.-Y., and Manga, M. (2015). New streams and springs after the 2014 Mw6.0 south napa earthquake. *Nat. Commun.* 6, 7597. doi:10.1038/ncomms8597

Wang, C.-y., Wang, C.-H., and Manga, M. (2004). Coseismic release of water from mountains: evidence from the 1999 (Mw = 7.5) chi-chi, taiwan, earthquake. *Geology* 32, 769–772. doi:10.1130/g20753.1

Xue, L., Li, H.-B., Brodsky, E. E., Xu, Z.-Q., Kano, Y., Wang, H., et al. (2013). Continuous permeability measurements record healing inside the Wenchuan earthquake fault zone. *Science* 340, 1555–1559. doi:10.1126/science.1237237

Zhu, W., Allison, K. L., Dunham, E. M., and Yang, Y. (2020). Fault valving and pore pressure evolution in simulations of earthquake sequences and aseismic slip. *Nat. Commun.* 11, 4833–4911. doi:10.1038/s41467-020-18598-z